



Article

SERS-Active Cu Nanoparticles on Carbon Nitride Support Fabricated Using Pulsed Laser Ablation

Hossein Dizajghorbani-Aghdam ¹, Thomas S. Miller ², Rasoul Malekfar ^{1,*} and Paul F. McMillan ^{3,*}

¹ Atomic and Molecular Group, Physics Department, Faculty of Basic Sciences, Tarbiat Modares University, Tehran 14115-175, Iran

² Electrochemical Innovation Lab, Department of Chemical Engineering, University College London, Torrington Place, London WC1E 7JE, UK

³ Department of Chemistry, Christopher Ingold Laboratories, University College London, 20 Gordon Street, London WC1H 0AJ, UK

* Correspondence: malekfar@modares.ac.ir (R.M.); p.f.mcmillan@ucl.ac.uk (P.F.M)

Received: 17 July 2019; Accepted: 23 August 2019; Published: 29 August 2019



Abstract: We report a single-step route to co-deposit Cu nanoparticles with a graphitic carbon nitride (gCN) support using nanosecond Ce:Nd:YAG pulsed laser ablation from a Cu metal target coated using acetonitrile (CH₃CN). The resulting Cu/gCN hybrids showed strong optical absorption in the visible to near-IR range and exhibited surface-enhanced Raman or resonance Raman scattering (SERS or SERRS) enhancement for crystal violet (CV), methylene blue (MB), and rhodamine 6G (R6G) used as probe analyte molecules adsorbed on the surface. We have characterized the Cu nanoparticles and the nature of the gCN support materials using a range of spectroscopic, structural, and compositional analysis techniques.

Keywords: pulsed laser ablation; acetonitrile (CH₃CN); Cu/gCN hybrids; localized surface plasmon resonance (LSPR); surface enhanced Raman scattering (SERS); surface enhanced resonance Raman scattering (SERRS)

1. Introduction

Surface-enhanced Raman spectroscopy (SERS) is a highly sensitive spectroscopic technique used to detect and study vibrational modes of molecules adsorbed on metal or semiconducting surfaces or nanoparticles (NP) [1–7]. SERS intensity enhancement factors (EFs) by up to 14 orders of magnitude arise from a combination of electromagnetic (EM) and chemical (CM) mechanisms [8,9]. EM enhancement factors ($\sim 10^7$ – 10^8) are dominant for metallic materials [10,11] compared with the CM enhancement ($\sim 10^3$) operating mainly among semiconductors [12–15]. Typical SERS active supports include noble metals (Au, Ag, Cu) that develop localized surface plasmon resonances (SPR) in the visible range, giving rise to the photon-vibrational coupling effects leading to SERS with EM enhancement [11,16]. In addition, if the adsorbed analyte contains a chromophore with a UV-visible absorption close to the SPR wavelength, additional enhancement can be observed due to resonance Raman (SERRS) effects [17].

Ag and Au NPs have been mainly investigated as the most highly active SERS substrates [11,18–21]. Cu NPs exhibit similar SPR properties but can show lower chemical stability toward adsorbate species [16,22–25]. Cu NPs are readily produced using solution chemistry techniques, but these approaches can lead to surface contamination due to atmospheric oxidation, as well as from the addition of surfactants such as polyethylene glycol, sodium dodecyl sulfate, etc. [26–28], thus hindering their use for SERS, as well as for biomedical and catalytic applications [29,30]. Laser ablation from

a pure metal target in the presence of a liquid medium has been shown to provide a useful alternative to obtain SERS-active NPs [24,25,31]. Using liquids such as H₂O or acetone results in the formation of Cu oxides [32–34] that reduce the SERS activity and affect the chemical stability [35]. Here, we explored the use of the oxygen-free liquids toluene (C₇H₈) and acetonitrile (CH₃CN) for the Cu laser ablation experiments. The aromatic hydrocarbon toluene produced Cu NPs surrounded by an amorphous carbon matrix that resulted in quenching of the SPR. Similar results have been reported for Au NPs [36,37]. These effects could be reduced by incorporating N atoms in the ablation medium and the resulting solid matrix surrounding and supporting the Cu NPs. Previous studies have described the laser ablation of Cu and other transition metal elements using acetonitrile to obtain metal NPs deposited along with a carbon nitride support, but the nature of the support material obtained has not yet been fully established [38–42]. Here, we characterized the Cu NPs and the carbon nitride matrix, that we established to have a polymeric to graphitic character based on mainly sp²-bonded C and N species (labelled gCN for convenience), using a range of spectroscopic, diffraction, and imaging techniques. We evaluated the performance of the Cu/gCN hybrid nanomaterials for their surface-enhanced Raman or resonance Raman scattering (SERS or SERRS) performance using crystal violet (CV), methylene blue (MB), and rhodamine 6G (R6G) as probe analyte molecules adsorbed on the NP surface.

Different classes of carbon nitride materials are currently being investigated for applications including catalysis, photocatalysis, electrochemical energy storage, and conversion, and as supports for catalytically active metal NPs [43–46]. Most work to date is focused on semiconducting compounds with C_xN_yH_z compositions and polymeric to layered (“graphitic”) structures are being developed. Although these materials are often cited as graphitic (g-) C₃N₄, this particular stoichiometry and layered structure have only been characterized in a single study that described a triazine-based graphitic carbon nitride (TGCN), produced using the polymerization of dicyandiamide (DCDA: C₂N₄H₄) in a LiCl:KCl molten salt medium [47]. That process normally results in crystalline polytriazine imide (PTI) solids containing intercalated Li⁺ and Cl[−] ions [48]; the TGCN material consisted of dark-colored flakes formed at the molten surface or deposited on the walls of the reaction vessel. However, related studies have found that the layered gCN materials deposited from above the DCDA/molten salt mixture under analogous reaction conditions had significantly greater C:N ratios, close to 1.3 [49,50]. That composition is similar to the gCN supports formed in our laser ablation study, described below. The wide range of materials described as carbon nitrides include N-doped graphite and graphene produced by chemical or physical vapor deposition exhibit semi-metallic to semiconducting behavior, with optoelectronic properties determined by the relative C:N ratio and their distribution within the sp²-bonded structures [51–53]. Such materials have been formed via the laser ablation of graphite targets in N₂ or NH₃ atmospheres, or by the laser-assisted reactions of precursors in gas and liquid media, giving rise to materials containing up to ≈20 at% nitrogen in the resulting amorphous to nanocrystalline films [54–60]. There have been reports of embedding Cu NPs in carbon nitride materials for functional applications. Hydrothermal processing in Cu-containing ionic liquids produced a Cu/gCN electrocatalyst that showed catalytic activity for the oxygen reduction reaction (ORR) critical for fuel cell operations [61], while reacting CuCl₂ with melamine in methanol formed supramolecular networks and carbon nitride nanosheets and nanorods with coordinated Cu²⁺ ions resulting in enhanced catalytic and visible light photocatalysis properties [62–66].

These last investigations indicate that electronic interactions between Cu NPs and supporting carbon nitride matrices can lead to the cooperative enhancement of catalytic and photocatalytic effects. Such interactions could be harnessed to develop other optical properties, including SERS enhancement of the vibrational signatures of molecular species adsorbed on the surface. Studies have reported combining semiconductor NPs (such as TiO₂) with plasmonically active NPs to stabilize and enhance the performance of SERS substrates [67–69]. Jiang et al. described a hybrid Ag/gCN material with a stable high-performance SERS activity, demonstrating strong optoelectronic interactions that promote the SERS enhancement along with charge transfer effects that protect the Ag NPs from oxidation [70,71]. Here we applied pulsed laser ablation of a Cu target coated with acetonitrile (CH₃CN) to create Cu/gCN

hybrid nanomaterials that were characterized using a range of spectroscopic, diffraction, and imaging techniques, and we studied their SERS/SERRS activity for the probe analyte molecules crystal violet (CV), methylene blue (MB), and rhodamine 6G (R6G).

2. Materials and Methods

A high-purity copper plate (Cu 99.98%) with a 2-mm thickness coated with acetonitrile served as the target for the laser ablation experiments. High-purity, methylene blue (MB), crystal violet (CV) (99.5%), and rhodamine 6G (R6G) ($\geq 95\%$) were purchased from Sigma Aldrich (Darmstadt, Germany) and used as SERS probe analytes. Bulk elemental analysis was carried out using an Elementar-Vario EL III system (Hanau, Germany) and X-ray photoelectron spectroscopy (XPS) was carried out using a Thermo Scientific K-Alpha instrument (Waltham Massachusetts, U.S.A) with a monochromated Al K α source (1486.6 eV). Transmission electron microscopy (TEM) was carried out using Zeiss-EM10C-80 kV (Germany) and JEOL JEM2010-200 kV (Tokyo, Japan) instruments. The micrographs were analyzed using ImageJ software (Version 6, California, U.S.A) [72] and by manual counting to determine the mean size of NPs in the TEM images. The average Cu NP sizes were determined to be ≈ 6 nm, slightly lower than those estimated from Scherrer broadening of the X-ray powder diffraction data. X-ray diffraction (XRD) patterns were recorded using an X-Pert MPD (Philips, Eindhoven, Netherlands) X-ray diffractometer with Co K α -radiation ($\lambda = 1.79026 \text{ \AA}$). Ultraviolet-visible (UV/vis) absorption spectra were obtained using a PG T80+ spectrophotometer (PG Instruments, Coventry, UK), Fourier Transform infrared (FTIR) spectra with a Thermo Nicolet NEXUS 670 FTIR (Waltham Massachusetts, U.S.A), and Raman spectroscopy including SERS or SERRS effects were recorded using a Thermo Nicolet Alpha spectrometer (Waltham Massachusetts, U.S.A) with a 532-nm excitation provided by a Nd:YLF laser.

Pulsed laser deposition was carried out using a Ce:Nd:YAG laser ($\lambda = 1064 \text{ nm}$) with a 10-ns pulse width and a 10-Hz repetition rate. The beam was focused on the Cu plate target using a 10-cm working distance lens. The target was fixed to the bottom of a glass cell and mounted on a rotator in order to avoid deep ablation. The laser pulse energy was held constant at 100 mJ/pulse. The typical diameter of the laser spot at the target was 2 mm and the acetonitrile level on the target surface was 2 mm. The pulsed laser was directed on the rotating target surface for 10 min to obtain a colloidal suspension of ablated nanomaterial particles. The suspension was then dried at 25 °C in air to provide solid powdered materials for further investigation.

To prepare SERS substrates, 1 mg of the synthesized support materials (Cu/gCN) were suspended in 5 mL of the different analyte solutions (CV, MB, and R6G) prepared with concentrations ranging between 10^{-3} – 10^{-8} mol/L in acetonitrile and stirred for 3 h to allow binding between the analyte and substrate. The analyte-decorated Cu/gCN solutions were centrifuged and washed multiple times with absolute acetonitrile to remove any unabsorbed analyte molecules and then the resulting powders were dispersed into 1 mL acetonitrile. SERS substrates were prepared by dropping aliquots of analyte-decorated Cu/gCN solutions (10 μL) onto a glass slide and the volatile liquid phase was left to evaporate at 25 °C in air to form a uniform coating. All Raman and SERS/SERRS experiments were carried out with the incident laser power maintained at 10 mW for a 60 μm (spot diameter) laser beam focused at different points on the sample surface maintaining a constant integration time of 100 s at a spectral resolution of 4 cm^{-1} . All spectra were measured using 532-nm excitation delivered by the second harmonic of a Nd:YLF laser and were collected in the range of 400–4000 cm^{-1} . All data processing and statistical analysis were carried out using the OMNIC™ software (Version 6) supplied by Thermo Nicolet (Waltham Massachusetts, U.S.A) and intensity values of the spectra were normalized according to the integration time within each data set.

3. Results and Discussion

3.1. Formation and Characterization of Cu/g-CN Materials Produced by Pulsed Laser Ablation in Acetonitrile

The interaction of high-power laser beams with a Cu target can result in several phenomena including heating, melting, and even vaporization of the surface, leading to the formation of plasma. A complex process involving adiabatic plasma expansion combined with shockwaves and the formation of cavitation bubbles result in ablation of Cu NPs that become suspended within the overlying liquid medium. The high temperatures generated by laser beam absorption using the Cu target result in bond-breaking and polymerization reactions occurring within the acetonitrile liquid phase surrounding the ablated metal NPs. Also, radiation from the laser-ablated Cu vapor plume leads to UV absorption and photolysis reactions within the acetonitrile liquid. The combination of these thermal and photolytic reaction effects, accompanied by new C–C/C–N bond formation, results in the formation of a polymerized gCN matrix that then surrounds and supports the Cu NPs formed during laser ablation treatment [38].

We first characterized the chemical composition of the Cu/gCN hybrid materials using bulk elemental (CNH) analysis that revealed a C:N ratio of 1.3, which was larger than those expected for g-C₃N₄ or polymeric to graphitic gCN materials prepared via the thermolysis of organic precursors [43,44]. However, it only slightly exceeded the C:N ratio found for layered gCN materials produced using vapor deposition above a molten salt bath from precursors such as DCDA [49,50]. Examination of the survey C1s and N1s spectra obtained from XPS measurements confirms this observation (Figure 1a–c). The C1s spectra could be fit using three mixed Gaussian–Lorentzian (GL) peaks at 284.3, 286.0, and 288.2 eV. The peak at 288.2 eV appears at a position that is characteristic of sp² C atoms bonded within a cyclic triazine or heptazine systems [44], although this constituted only a minor (5.5%) component of the overall C contribution. The peak at 286.0 eV (18.55% of the C contribution) was assigned to C–N bonded species, although it might also contain a contribution from C–O bonded species that are often recorded for gCN materials due to surface oxidation [44,50]. It is probable that the remainder of the C–N bonding was represented by a significant, but unresolvable, contribution to the peak at 284.3 eV, along with a component from adventitious carbon [50,53]. The presence of the C1s peak at 286.0 eV, as well as a significant proportion of that observed at 284.3 eV, confirmed the presence of significant C–N interactions within the sample. The N1s spectrum (Figure 1c) was best fit with two GL peaks, one at 398.4 eV, and a second contribution at 399.5 eV. The smaller peak resembles that observed for melamine and is usually interpreted to be indicative of C–N–H uncondensed amino (–NH₂) groups [44]. We note that the IR spectra discussed below indicate the presence of N–H bonded species. The peak at the higher binding energy (BE) resulted from the remaining C–N species, which included C–N=C bonded units indicated by the peak in the C1s spectrum. The IR and Raman data also indicated the presence of terminal nitrile (–C≡N) units that contributed to the N1s signal. The C1s:N1s peak ratio found from the XPS data was 4.76. This was significantly larger than the value determined using bulk elemental analysis (1.33), but it was certainly affected by a significant contribution from adventitious carbon. However, the fact that the C:N ratio was substantially greater than 1 clearly indicates that both C–C and C–N species were present within the gCN materials. The Cu 2p_{3/2} peak (Figure 1d) exhibits a single sharp feature that could be fitted using a GL peak at 933.3 eV. The shape and position of this feature, as well as the absence of higher BE satellites, rule out the presence of Cu(II), but Cu(I) and Cu(0) species both have similar XPS signatures, and it is possible that either or both of these species might be present within the sample [73].

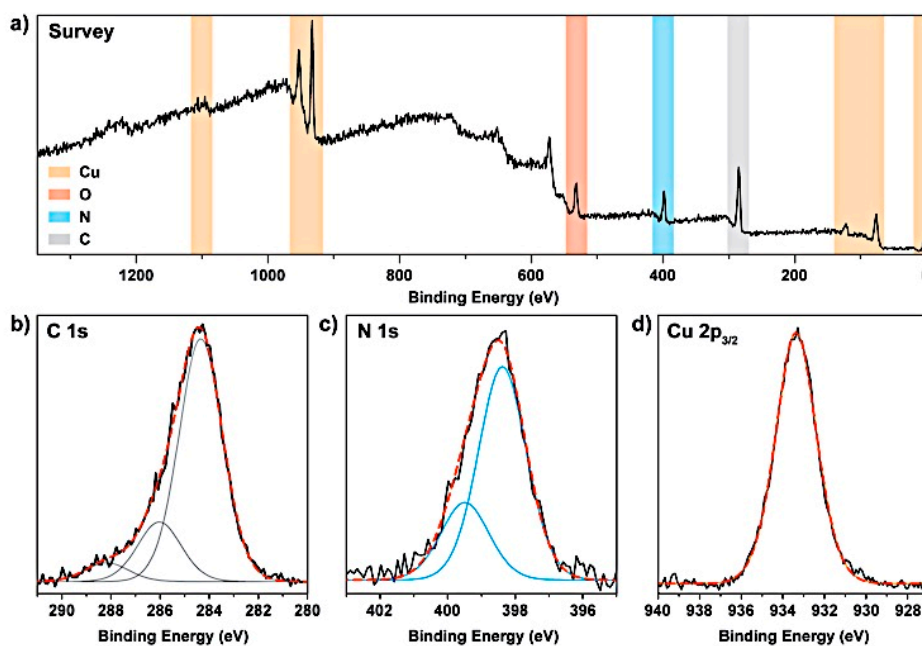


Figure 1. (a) XPS survey spectrum, (b) C1s, (c) N1s, and (d) Cu 2p_{3/2} XPS spectra of the Cu/gCN material produced by laser ablation under acetonitrile.

UV-visible absorption spectra of the Cu/gCN nanomaterials obtained in suspension in acetonitrile following the laser ablation synthesis exhibited a peak at ≈ 580 nm due to the localized surface plasmon resonance (SPR) band of the Cu NPs (Figure 2) [16,24,74].

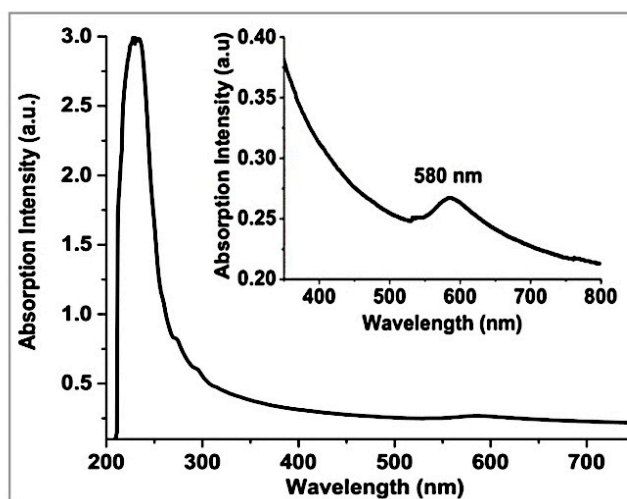


Figure 2. UV-visible absorption spectrum of a typical Cu/gCN nanomaterial synthesized using pulsed laser ablation in acetonitrile. The inset shows a vertically expanded region of the spectrum around the position of the surface plasmon resonance for Cu NPs.

The XRD pattern of dried powders obtained using Co K α radiation showed weak sharp peaks that were distinct from the broad and more intense features from the amorphous gCN matrix (Figure 3). The weak peaks occurring at 50.7° and 59.2° 2θ ($\lambda = 1.79026$ Å) were identified with the {111} and {200} reflections of crystalline Cu (2.09 and 1.08 Å, respectively). A very weak feature could just be distinguished at 89.1° 2θ (1.27 Å) that corresponded to the {220} reflection. Examining the widths of these features indicated an NP size with an average mean diameter ≈ 32 nm estimated using Scherrer's formula (Table 1). The pattern was dominated by a strong, broad peak at 34.3° 2θ (3.03 Å), along with

a weaker feature at $28.9^\circ 2\theta$ (3.59 \AA). These resembled the broad reflections observed for polymeric to graphitic carbon nitride materials prepared using thermolysis of organic precursors, where they are commonly interpreted in relation to the $\{002\}$ and $\{100\}$ planes of polytriazine to polyheptazine graphitic layered structures, even though the actual materials are known to be incompletely polymerized and contain ribbon-like units along with partially formed sheets [44,75–77]. Similar features were also found for nanocrystalline layered materials with higher C:N ratios close to those observed for the gCN supports created in this study [44,49,50]. We note, however, that the main XRD peak occurred at a value that is $\approx 11\%$ smaller than the interplanar d_{002} spacing of crystalline graphite ($d_{002} = 3.28 \text{ \AA}$), or gCN compounds with both low ($\sim 3.26 \text{ \AA}$) and high C:N ratios ($\sim 3.24 \text{ \AA}$) [44,49,50,75–77].

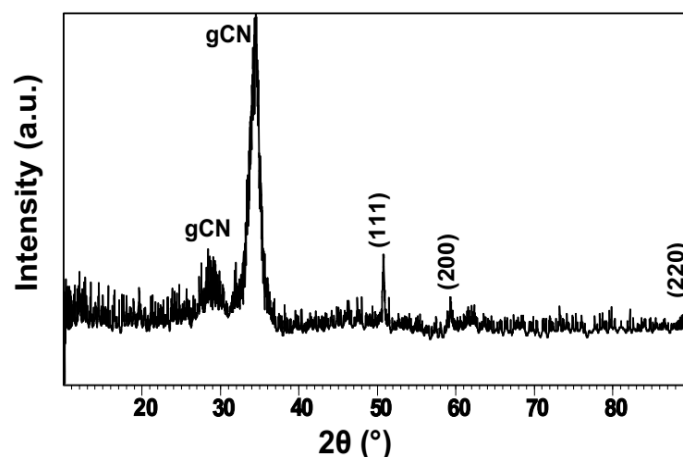


Figure 3. Powder XRD pattern (obtained using Co $K\alpha$ radiation, $\lambda = 1.79026 \text{ \AA}$) of the Cu/gCN material formed using pulsed laser ablation in acetonitrile. The weak sharp peaks due to crystalline Cu NPs are labeled with their $\{hkl\}$ values. The strong broad features are due to the gCN support generated during the laser ablation synthesis from acetonitrile.

Table 1. Summary of X-ray diffraction data obtained using Co $K\alpha$ radiation ($\lambda = 1.79026 \text{ \AA}$) for a typical Cu/gCN material prepared using pulsed laser ablation in acetonitrile. * The assignment of peaks for gCN is discussed in the text.

Angle (2θ)	$\{hkl\}$	FWHM (2θ)	d-spacing (\AA)	Height (counts)	Identification
28.9	*	3.3	3.59	27.2	gCN
34.3	*	1.6	3.03	153.9	gCN
50.7	$\{111\}$	0.3	2.09	36.9	Cu
59.2	$\{200\}$	0.4	1.08	14.6	Cu
89.1	$\{220\}$	3.2	1.27	5.4	Cu

Cu NPs were shown to be distributed throughout the gCN matrix via TEM imaging (Figure 4a–d). By counting ≈ 40 particles, the mean diameter was found to be $\approx 6 \text{ nm}$ by analyzing the images using ImageJ software [72]. A few particles in the field of view were observed to have diameters in the 10–25 nm range. The greater average particle size ($\approx 30 \text{ nm}$) indicated using the XRD results could have been the result of the presence of large NPs within the bulk materials that were not sampled in the TEM experiments, although Scherrer analysis of the X-ray peaks is not always reliable. The gCN supporting matrix revealed a turbostratic texture with an "onion-like" structure developed around the Cu NPs (Figure 4c).

FTIR spectra of a pressed KBr disc of the powdered Cu/gCN sample contained a strong band at 3340 cm^{-1} due to N–H stretching from the gCN material, combined with a contribution from O–H stretching from surface-adsorbed H_2O (Figure 5a) [78,79]. The peak at 1640 cm^{-1} was due to molecular H_2O bending vibrations [78]. The features at $2850\text{--}2950 \text{ cm}^{-1}$ indicated the presence of sp^3 -hybridized C–H bonds [80]. Features in the $1000\text{--}1450 \text{ cm}^{-1}$ region can be assigned to C–N and

possibly C–O stretching vibrations [44,50]. The sharp peak at 2120 cm^{-1} was due to terminal $\text{C}\equiv\text{N}$ bond stretching within the incompletely condensed carbon nitride matrix [79,80]. The strong Raman peak at 2155 cm^{-1} confirmed this assignment (Figure 5b), although it is not clear why there should be a 35 cm^{-1} difference between the IR and Raman data. This could indicate a vibrational interaction between adjacent nitrile groups within the structure giving rise to symmetric and antisymmetric combinations; however, typically the IR mode should occur at a higher wavenumber. Our observation of this feature clearly indicates that the gCN material produced by laser ablation from acetonitrile was not fully polymerized into graphitic sheets. However, the sharp peak in the IR spectrum near 810 cm^{-1} was typical of breathing modes of ring units in carbonaceous and C_xN_y materials. Also, the Raman spectrum contained two main bands at 1346 and 1540 cm^{-1} that resembled the “G” and “D” bands of disordered graphite, amorphous carbon, and graphitic carbon nitride materials, associated with C–N/C–C stretching vibrations within the gCN matrix [44,50,79,80].

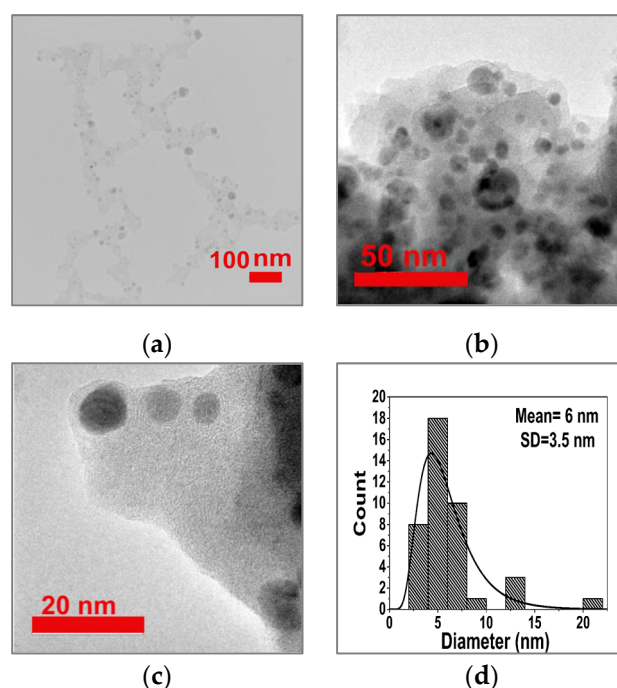


Figure 4. TEM images of Cu NPs embedded in the amorphous gCN support. (a) Low-resolution image obtained using a Zeiss-EM10C-80 kV instrument; (b,c) High-resolution images obtained using a JEOL JEM2010-200 kV TEM. (d) Mean size (nm) and distribution by analysis of ≈ 40 Cu NPs.

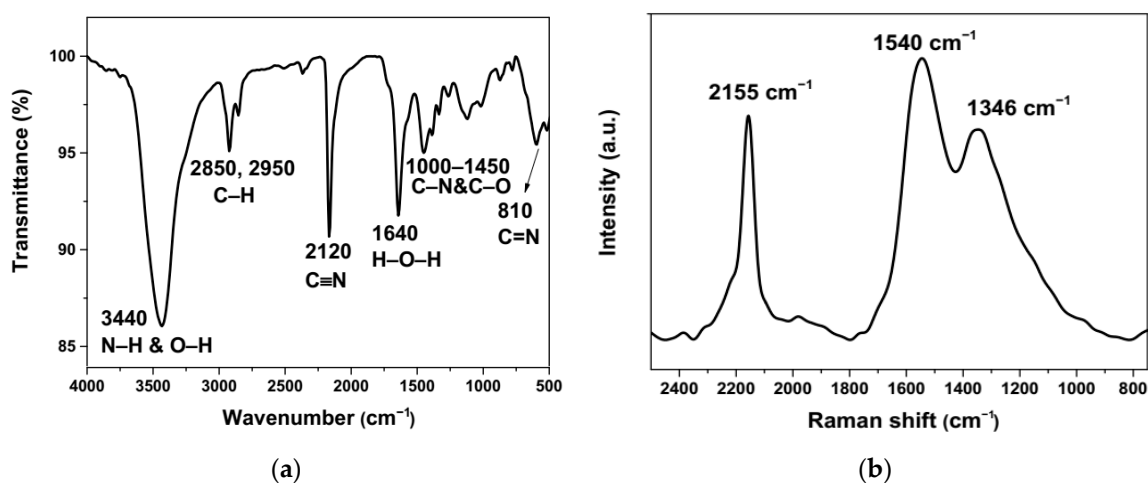


Figure 5. (a) FTIR and (b) Raman spectra of Cu/gCN hybrid material synthesized using pulsed laser ablation in acetonitrile.

3.2. SERS/SERRS Activity of Analytes on Cu/gCN Hybrid Support Produced Using Pulsed Laser Deposition

We tested the SERS/SERRS activity of the CuNP/g-CN hybrid using the dye molecules CV, MB, and R6G as analyte probes. A drop of each the analyte-decorated Cu/gCN solutions prepared with various due concentrations (10^{-3} – 10^{-7} M) was placed on the prepared glass slide substrates separately and allowed to dry before recording surface-enhanced spectra. “Normal” and SERS/SERRS spectra are compared in Figure 6, after subtraction of the background fluorescence (Figure S1). No additional bands were observed from the gCN support material (Figure S2). All spectra were obtained using a total integration time of 100 s from 50 accumulated scans with a 2-s exposure. The spectra shown in Figure 6 have been displaced vertically to more clearly show the SERS/SERRS enhancement.

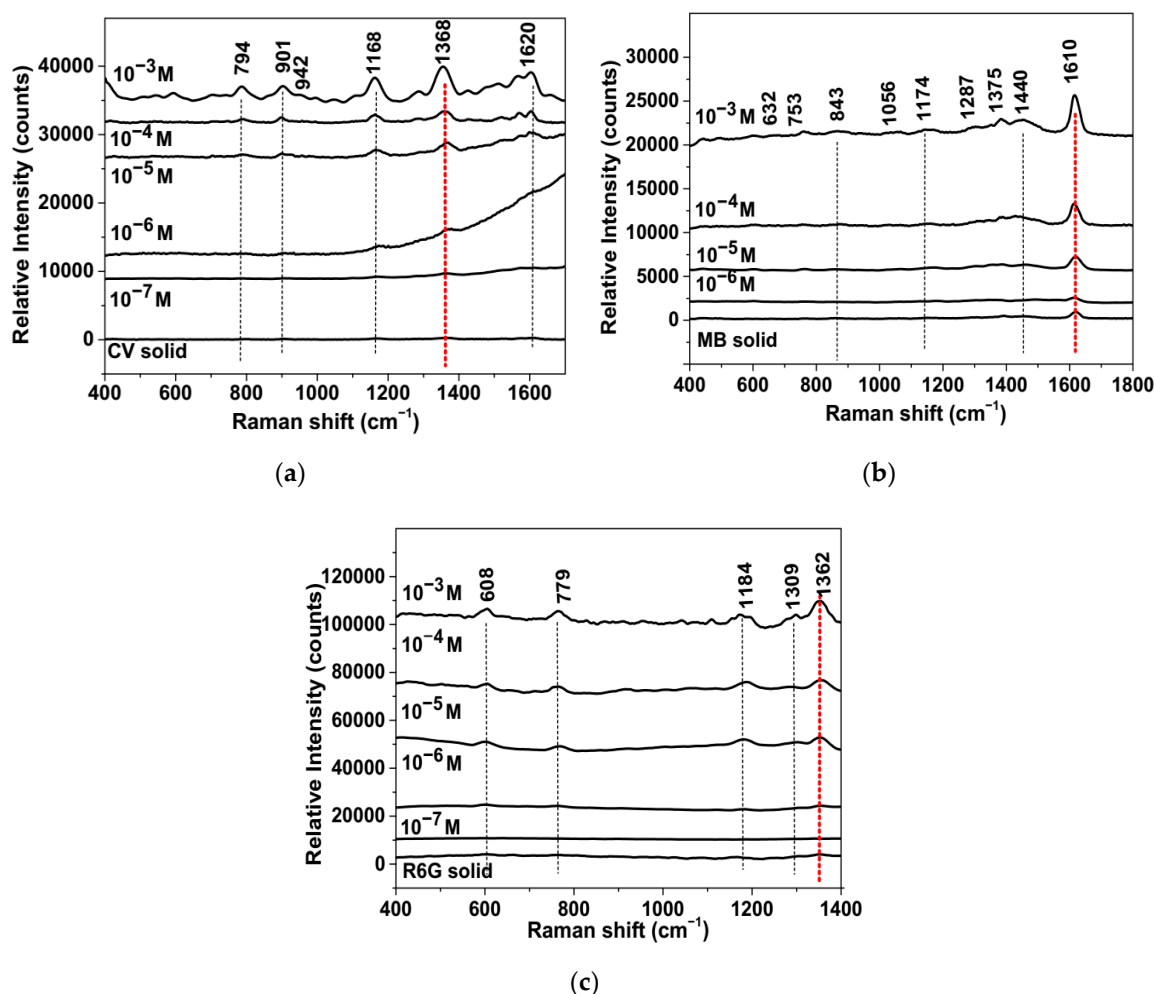


Figure 6. Raman spectra of (a) CV, (b) MB, and (c) R6G powders compared with SERS/SERRS spectra of the analytes with different concentrations decorated on a Cu/g-CN substrate. All spectra were plotted following baseline subtraction (see Figure S1). The red line indicates the characteristic peak used to determine the SERS activity (see text and Supporting Information). The spectra have been vertically displaced for clarity. The counts shown correspond to an integration time of 100 s of 50 accumulated scans, each with a 2-s exposure period. We note that for the CV sample prepared with a 10^{-7} M concentration, an additional fluorescence background contribution remained that was not fully accounted for by the baseline subtraction procedure. This was most likely due to some analyte molecules that were not completely removed from the underlying glass support by the washing procedure.

Because CV has a main UV-visible absorption band extending between 420–640 nm with its principal maximum near 580 nm, resonance Raman (RR) effects were expected to occur for the bulk crystalline sample using 532 nm excitation [81]. However, using the acquisition conditions applied

here, we could barely observe the vibrational peaks of CV rising above the background when presented at the same vertical expansion as the SERS/SERRS spectra (Figure 6a). For the analyte deposited on the Cu/gCN support at 10^{-3} M concentration, we clearly observed the spectrum of CV with peaks at 794, 901, 942, 1168, 1368, and 1620 cm^{-1} (Figure 6a). Although the positions and relative intensities generally resembled those of published spectra of the solid sample obtained with different laser wavelengths [81], we observed the most significant enhancement in the intensity of the feature at 1368 cm^{-1} that contains a main contribution from symmetric ϕ -N (ϕ = phenyl) stretching [81]. As the concentration of adsorbed CV molecules was reduced by decadic amounts, the main peaks could still be clearly distinguished from the background down to 10^{-7} M (Figure 6a).

MB exhibited a UV-visible absorption that had barely begun at the 532 nm laser wavelength, and so it was expected that any RR or pre-resonance effects would be minimal for the bulk sample, while the background fluorescence should be low [82]. That was consistent with our data for the solid sample, for which the principal peak recorded at $\approx 1610\text{ cm}^{-1}$ in our study was clearly observed for the counting conditions used here (Figure 6b). However, the Cu NP SPR occurred at 580 nm, which lay within the electronic absorption profile of the chromophore, and so the SERS enhancement effects could also include SERRS. We observed SERS-active Raman peaks at 632, 753, 843, 1056, 1174, 1287, 1375, 1440, and 1610 cm^{-1} for our sample prepared from a 10^{-3} M analyte solution, with a relative intensity pattern that resembled that obtained by Anastasopolous et al. for MB molecules at 10^{-4} M concentration adsorbed on Ag NPs and excited using a 514.5 nm excitation [82]. We can clearly observe the dominant 1610 cm^{-1} peak down to a 10^{-6} M concentration, with a relative intensity that was only slightly lower than that for the bulk solid (Figure 6b).

R6G exhibited an electronic absorption maximum at 530 nm that matched the laser excitation wavelength and also lay close to the SPR of Cu NPs, and so RR effects were expected to be observed for both the bulk solid and adsorbed molecules in our study using a 532-nm laser excitation. As observed by previous researchers, the SERRS effect on Au nanoparticles or roughened Cu surfaces resulted in the appearance of the characteristic Raman peaks of the adsorbed molecules using red (632.8 nm) to blue (488 nm) excitation lines [83,84]. Our data show that the spectrum could be detected down to at least 10^{-6} M, where the relative intensities were comparable to those of the bulk solid (Figure 6c). Overall, our results demonstrated that the Cu/g-CN hybrid substrate exhibited good SERS/SERRS sensitivity for the CV, MB, and R6G molecular analytes.

3.3. Estimation of SERS/SERRS Enhancement Factors

In order to further investigate the SERS/SERRS enhancement activities of the Cu/gCN substrate, the surface was decorated with a sufficiently high concentration of analyte molecules (CV, MB, and R6G, 10^{-3} M) to ensure full a monolayer coverage of the NP surface. We assumed that the probe molecules were uniformly adsorbed on the support surfaces. The relative intensities of characteristic peaks for the three molecules were then compared with those obtained from a dried spot ($2\text{ }\mu\text{L}$; $\approx 10\text{ mm}^2$) of pure analyte solution prepared at the same concentration (Figure 7a–c). The peaks at 1368, 1610, and 1362 cm^{-1} were considered for CV, MB, and R6G analytes, respectively. SERS/SERRS enhancement factors (EFs) were then estimated using the following equation [85–87]:

$$EF = (I_{SERS}/n_{SERS})/(I_{Raman}/n_{Raman}) \quad (1)$$

Here, n_{Raman} and n_{SERS} were the number of analyte molecules included within the laser beam sampling volume for the normal Raman and SERS samples, respectively. I_{SERS} and I_{Raman} were the absolute intensity values measured for the same mode in the Raman and SERS/SERRS spectra of the analyte. The area of the laser illumination (A_{laser}) constituted a circle $\approx 30\text{ }\mu\text{m}$ in radius (r_{laser}). The focused laser beam penetrated $\approx 4\text{ }\mu\text{m}$ into the material [86,88]. We considered the Cu NPs to be spherical with a radius (r_{NP}) of $\approx 16\text{ nm}$ (estimated from the XRD and TEM results), and that the particles were half-way embedded into the gCN matrix. We neglected spaces between the NPs.

The number of analyte molecules illuminated by the laser beam for the solid and SERS samples were then obtained using:

$$n_{SERS} = (n_{NPs} \cdot A_{NP}) / (A_{Analyte}) \quad (2)$$

Here, n_{NPs} , A_{NP} , and $A_{Analyte}$ were the number of NPs in the area illuminated by the laser, the surface area per NP, and the analyte molecule surface area, respectively. n_{Raman} was then obtained using the following relation:

$$n_{Raman} = (N_A \cdot V_{Analyte} \cdot d_{Analyte}) / (M_{Analyte}) \quad (3)$$

where N_A is Avogadro's number, and $V_{Analyte}$, $d_{Analyte}$, and $M_{Analyte}$ were the effective volume of analyte in the laser beam, the density, and molecular weights of the related analyte (Table 2), respectively. The EFs were then estimated using Equation (1) for the different analytes (Table 2). The determined values were $\approx 7.2 \times 10^7$, 2.3×10^7 , and 1.3×10^7 for the CV, MB, and R6G analytes on the Cu/gCN substrate, respectively (see Method S1 for further details).

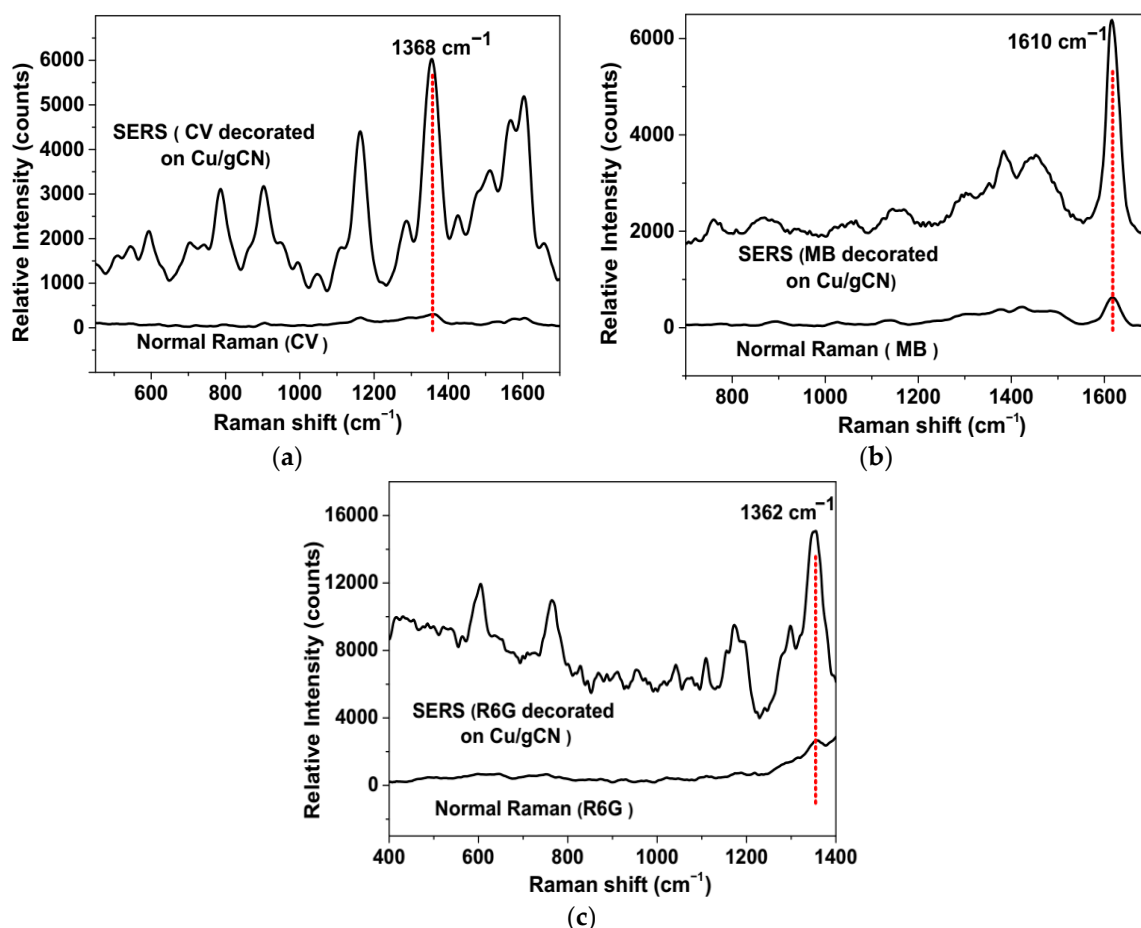


Figure 7. Comparison of the “normal” (i.e., non-SERS) Raman spectra of (a) CV, (b) MB, and (c) R6G with the SERS/SERRS spectra of the three analytes decorated on a Cu/gCN support. The concentration of the analytes was 10^{-3} M for recording both the “normal” Raman and SERS spectra. Spectra were plotted following subtraction of the fluorescence background from the organic molecules (see Figure S1). The red line indicates the characteristic peak used to determine the SERS activity (see text and Supporting Information). The spectra have been vertically displaced for clarity. The counts represent an integration time of 100 s of 50 accumulated scans, each with a 2 s exposure period in all cases.

Table 2. Physical characteristics of the analytes used to estimate *EFs*.

Analyte	Density (g/mL)	Surface Area (nm ²)	n_{Raman}/n_{SERS}	I_{SERS}/I_{Raman}	Cu/g-CN <i>EFs</i>
Crystal violet	1	1.2	$5.4 \times 10^{15}\pi/1.5 \times 10^9\pi$	20	7.2×10^7
Methylene blue	0.98	1.3	$6.6 \times 10^{15}\pi/1.4 \times 10^9\pi$	6.6	2.3×10^7
Rhodamine 6G	1.26	0.6	$6 \times 10^{15}\pi/3 \times 10^9\pi$	6.4	1.3×10^7

Because of the several assumptions and approximations used to obtain these *EFs*, they can only be considered as guide values for comparison with SERS and SERRS *EF* values recorded for these and related analytes on noble metal nanoparticles supported on semiconducting surfaces. Su et al. prepared a Au/MoS₂ nanocomposite using in situ growth of Au NPs on MoS₂ nanosheet surfaces, and demonstrated that the Au@MoS₂ substrates exhibited an 8.2×10^5 enhancement for the 1362 cm⁻¹ Raman mode of R6G [89]. Jiang et al. reported that g-C₃N₄/Ag NPs exhibited *EFs* of 4.6×10^8 and 2.1×10^9 using CV as an analyte [70,71]. These authors linked the large *EF* values to multiple enhancement contributions, and that charge transfer between the g-C₃N₄ and the metal surface protected the Ag NPs from oxidation. There are only a few literature reports on the use of pure Cu NPs as a SERS substrate, either supported or in colloidal suspension [16,23–25]. Dendisová-Vyškovská et al. found *EF* = 1.7×10^5 for the 1590 cm⁻¹ band of 4-aminobenzenethiol (4-ABT) [16], and Ding et al. obtained an *EF* = 1.6×10^7 for CV adsorbed on an array of Cu NPs deposited using sputtering on the surface of a monolayered colloidal crystal of 350 nm polystyrene spheres [23]. The SERS/SERRS results varied dramatically as a function of NP size controlled by the deposition time, with the most intense spectra recorded for an 18 min deposition with particles ≈ 150 –200 nm in size. Although the exciting wavelength (532 nm) was the same as that used in our study, the SERS/SERRS spectrum recorded for CV was slightly different to our result in that the 1619 cm⁻¹ band was much more intense. However, the fact that the *EFs* obtained in both studies is comparable is encouraging.

4. Conclusions

Our results confirm that Cu/gCN nanomaterial composites can be useful for the development of SERS/SERRS applications. Our Cu NPs on sp²-bonded carbon nitride supports were fabricated using pulsed laser ablation of a Cu plate immersed in acetonitrile solvent. We carried out chemical, structural, and spectroscopic analyses to study the nature of the Cu NPs and their gCN support. The N:C ratio of the gCN material determined using bulk analysis was ≈ 1.3 , significantly lower than the semiconducting carbon nitride compounds based on heptazine- to triazine-based structures, but it contained close-to-layered gCN materials containing mixed C–N/C–C bonding prepared using vapor deposition techniques. Such materials might contain locally electronically conducting domains. The degree of layer polymerization was incomplete, as shown by strong IR and Raman signals from terminal C \equiv N bonds. The Cu/gCN hybrid nanocomposites exhibited strong visible absorption extending toward the near-IR region with an SPR signal from the metal NPs at 580 nm. SERS/SERRS enhancement activity was tested using three analyte molecules (CV, MB, and R6G) prepared with initial solution concentrations of 10^{-3} – 10^{-7} mol/L in acetonitrile and adsorbed onto the Cu/gCN nanocomposite surfaces. The observed SERS/SERRS enhancement factors were on the order of 10^7 , comparable with *EF* values found for nanoparticle arrays of Cu produced using sputtering onto templates and other noble metal NPs supported by gCN materials. Further studies are now needed to investigate the possibility of cooperative interactions between the gCN support and the metal NPs that could enhance the optoelectronic effects leading to SERS/SERRS enhancement, as well as in stabilizing the Cu NPs.

Supplementary Materials: The Supplementary Materials are available online at <http://www.mdpi.com/2079-4991/9/9/1223/s1>.

Author Contributions: The study was devised by R.M. and synthesis, Raman, and SERS experiments were performed by H.D.-A. TEM and XPS characterization was performed by T.S.M. All authors participated in the interpretation of the results. H.D.-A. wrote a first draft of the manuscript that was completed and edited by P.F.M. and T.S.M.

Funding: R.M. thanks the Iran Nanotechnology Initiative Council (INIC) for financial support of the pulsed laser ablation setup. P.F.M. acknowledges support from the EU Graphene Flagship under Horizon 2020 Research and Innovation program grant agreement No. 696656—Graphene Core2. T.S.M. thanks the UK Engineering Physical Research Council for support via the EPSRC Postdoctoral Fellowship EP/P023851/1.

Conflicts of Interest: The authors declare no conflict of interest. The funders had no role in the design of the study; in the collection, analyses, or interpretation of data; in the writing of the manuscript, or in the decision to publish the results.

References

1. Bell, S.E.J.; Sirimuthu, N.M.S. Surface-Enhanced Raman Spectroscopy (SERS) for Sub-Micromolar Detection of DNA/RNA Mononucleotides. *J. Am. Chem. Soc.* **2006**, *128*, 15580–15581. [[CrossRef](#)] [[PubMed](#)]
2. Ambrosio, R.C.; Gewirth, A.A. Characterization of Water Structure on Silver Electrode Surfaces by SERS with Two-Dimensional Correlation Spectroscopy. *Anal. Chem.* **2010**, *82*, 1305–1310. [[CrossRef](#)] [[PubMed](#)]
3. Roguska, A.; Kudelski, A.; Pisarek, M.; Lewandowska, M.; Kurzydłowski, K.; Janik-Czachor, M. In situ spectroelectrochemical surface-enhanced Raman scattering (SERS) investigations on composite Ag/TiO₂-nanotubes/Ti substrates. *Surf. Sci.* **2009**, *603*, 2820–2824. [[CrossRef](#)]
4. Qiu, C.; Zhang, L.; Wang, H.; Jiang, C. Surface-Enhanced Raman Scattering on Hierarchical Porous Cuprous Oxide Nanostructures in Nanoshell and Thin-Film Geometries. *J. Phys. Chem. Lett.* **2012**, *3*, 651–657. [[CrossRef](#)] [[PubMed](#)]
5. Fateixa, S.; Nogueira, H.I.S.; Trindade, T.; Caria, S.F.; Nogueira, H.S. Hybrid nanostructures for SERS: Materials development and chemical detection. *Phys. Chem. Chem. Phys.* **2015**, *17*, 21046–21071. [[CrossRef](#)] [[PubMed](#)]
6. Han, X.X.; Ji, W.; Zhao, B.; Ozaki, Y. Semiconductor-enhanced Raman scattering: Active nanomaterials and applications. *Nanoscale* **2017**, *9*, 4847–4861. [[CrossRef](#)] [[PubMed](#)]
7. Lombardi, J.R.; Birke, R.L. A Unified Approach to Surface-Enhanced Raman Spectroscopy. *J. Phys. Chem. C* **2008**, *112*, 5605–5617. [[CrossRef](#)]
8. Kneipp, K.; Wang, Y.; Kneipp, H.; Perelman, L.T.; Itzkan, I.; Dasari, R.R.; Feld, M.S. Single Molecule Detection Using Surface-Enhanced Raman Scattering (SERS). *Phys. Rev. Lett.* **1997**, *78*, 1667–1670. [[CrossRef](#)]
9. Nie, S.; Emory, S.R. Probing single molecules and single nanoparticles by SERS. *Science* **1997**, *275*, 1102–1106. [[CrossRef](#)] [[PubMed](#)]
10. Xu, H.; Bjerneld, E.J.; Käll, M.; Börjesson, L. Spectroscopy of Single Hemoglobin Molecules by Surface Enhanced Raman Scattering. *Phys. Rev. Lett.* **1999**, *83*, 4357–4360. [[CrossRef](#)]
11. Schlücker, S. Surface-Enhanced Raman Spectroscopy: Concepts and Chemical Applications. *Angew. Chem. Int. Ed.* **2014**, *53*, 4756–4795. [[CrossRef](#)] [[PubMed](#)]
12. Wang, X.; Shi, W.; She, G.; Mu, L. Using Si and Ge Nanostructures as Substrates for Surface-Enhanced Raman Scattering Based on Photoinduced Charge Transfer Mechanism. *J. Am. Chem. Soc.* **2011**, *133*, 16518–16523. [[CrossRef](#)] [[PubMed](#)]
13. Ji, W.; Zhao, B.; Ozaki, Y. Semiconductor materials in analytical applications of surface-enhanced Raman scattering. *J. Raman Spectrosc.* **2016**, *47*, 51–58. [[CrossRef](#)]
14. Musumeci, A.; Gosztola, D.; Schiller, T.; Dimitrijevic, N.M.; Mujica, V.; Martin, D.; Rajh, T. SERS of Semiconducting Nanoparticles (TiO₂Hybrid Composites). *J. Am. Chem. Soc.* **2009**, *131*, 6040–6041. [[CrossRef](#)] [[PubMed](#)]
15. Teguh, J.S.; Xing, B.; Yeow, E.K.L.; Liu, F.; Xing, P.D.B.; Yeow, P.D.E.K.L. Surface-Enhanced Raman Scattering (SERS) of Nitrothiophenol Isomers Chemisorbed on TiO₂. *Chem. Asian J.* **2012**, *7*, 975–981. [[CrossRef](#)] [[PubMed](#)]

16. Dendisova-Vyskovska, M.; Prokopec, V.; Člupek, M.; Matějka, P. Comparison of SERS effectiveness of copper substrates prepared by different methods: What are the values of enhancement factors? *J. Raman Spectrosc.* **2012**, *43*, 181–186. [[CrossRef](#)]
17. McNay, G.; Eustace, D.; Smith, W.E.; Faulds, K.; Graham, D. Surface-enhanced Raman scattering (SERS) and resonance Raman scattering (SERRS): A review of applications. *Appl. Spectrosc.* **2011**, *65*, 825–837. [[CrossRef](#)] [[PubMed](#)]
18. Bell, S.E.J.; McCourt, M.R. SERS enhancement by aggregated Au colloids: Effect of particle size. *Phys. Chem. Chem. Phys.* **2009**, *11*, 7455–7462. [[CrossRef](#)] [[PubMed](#)]
19. Jung, M.; Kim, S.K.; Lee, S.; Kim, J.H.; Woo, D. Ag nanodot array as a platform for surface-enhanced Raman scattering. *J. Nanophotonics* **2013**, *7*, 073798. [[CrossRef](#)]
20. Jung, G.B.; Bae, Y.M.; Lee, Y.J.; Ryu, S.H.; Park, H.-K. Nanoplasmonic Au nanodot arrays as an SERS substrate for biomedical applications. *Appl. Surf. Sci.* **2013**, *282*, 161–164. [[CrossRef](#)]
21. Ameer, F.S.; Pittman, C.U.; Zhang, D. Quantification of Resonance Raman Enhancement Factors for Rhodamine 6G (R6G) in Water and on Gold and Silver Nanoparticles: Implications for Single-Molecule R6G SERS. *J. Phys. Chem. C* **2013**, *117*, 27096–27104. [[CrossRef](#)]
22. Roguska, A.; Kudelski, A.; Pisarek, M.; Opara, M.; Janik-Czachor, M. Surface-enhanced Raman scattering (SERS) activity of Ag, Au and Cu nanoclusters on TiO₂ -nanotubes/Ti substrate. *Appl. Surf. Sci.* **2011**, *257*, 8182–8189. [[CrossRef](#)]
23. Ding, Q.; Hang, L.; Ma, L. Controlled synthesis of Cu nanoparticle arrays with surface enhanced Raman scattering effect performance. *RSC Adv.* **2018**, *8*, 1753–1757. [[CrossRef](#)]
24. Nguyen, T.B.; Vu, T.K.T.; Nguyen, Q.D.; Nguyen, T.D.; Nguyen, T.A.; Trinh, T.H. Preparation of metal nanoparticles for surface enhanced Raman scattering by laser ablation method. *Adv. Nat. Sci. Nanosci. Nanotechnol.* **2012**, *3*, 025016. [[CrossRef](#)]
25. Muniz-Miranda, M.; Gellini, C.; Giorgetti, E. Surface-Enhanced Raman Scattering from Copper Nanoparticles Obtained by Laser Ablation. *J. Phys. Chem. C* **2011**, *115*, 5021–5027. [[CrossRef](#)]
26. Khan, A.; Rashid, A.; Younas, R.; Chong, R. A chemical reduction approach to the synthesis of copper nanoparticles. *Int. Nano Lett.* **2016**, *6*, 21–26. [[CrossRef](#)]
27. Soomro, R.A.; Sirajuddin, S.T.H.S.; Memon, N.; Shah, M.R.; Kalwar, N.H.; Hallam, K.R.; Shah, A. Synthesis of Air Stable Copper Nanoparticles and Their Use in Catalysis. *Adv. Mater. Lett.* **2014**, *5*, 191–198. [[CrossRef](#)]
28. Dang, T.M.D.; Le, T.T.T.; Fribourg-Blanc, E.; Dang, M.C. Synthesis and optical properties of copper nanoparticles prepared by a chemical reduction method. *Adv. Nat. Sci. Nanosci. Nanotechnol.* **2011**, *2*, 015009. [[CrossRef](#)]
29. Matikainen, A.; Nuutinen, T.; Itkonen, T.; Heinlehto, S.; Puustinen, J.; Hiltunen, J.; Lappalainen, J.; Karioja, P.; Vahimaa, P. Atmospheric oxidation and carbon contamination of silver and its effect on surface-enhanced Raman spectroscopy (SERS). *Sci. Rep.* **2016**, *6*, 37192. [[CrossRef](#)]
30. Zeng, F.; Xu, D.; Zhan, C.; Liang, C.; Zhao, W.; Zhang, J.; Feng, H.; Ma, X. Surfactant-Free Synthesis of Graphene Oxide Coated Silver Nanoparticles for SERS Biosensing and Intracellular Drug Delivery. *ACS Appl. Nano Mater.* **2018**, *1*, 2748–2753. [[CrossRef](#)]
31. Neddersen, J.; Chumanov, G.; Cotton, T.M. Laser Ablation of Metals: A New Method for Preparing SERS Active Colloids. *Appl. Spectrosc.* **1993**, *47*, 1959–1964. [[CrossRef](#)]
32. Gondal, M.A.; Qahtan, T.F.; Dastageer, M.A.; Maganda, Y.W.; Anjum, D.H. Synthesis of Cu/Cu₂O nanoparticles by laser ablation in deionized water and their annealing transformation into CuO nanoparticles. *J. Nanosci. Nanotechnol.* **2013**, *13*, 5759–5766. [[CrossRef](#)] [[PubMed](#)]
33. Aghdam, H.D.; Azadi, H.; Esmaeilzadeh, M.; Bellah, S.M.; Malekfar, R. Ablation time and laser fluence impacts on the composition, morphology and optical properties of copper oxide nanoparticles. *Opt. Mater.* **2019**, *91*, 433–438. [[CrossRef](#)]
34. Abdulateef, S.A.; MatJafri, M.Z.; Omar, A.F.; Ahmed, N.M.; Azzez, S.A.; Ibrahim, I.M.; Al-Jumaili, B.E.B. Preparation of CuO nanoparticles by laser ablation in liquid. *AIP Conf. Proc.* **2016**, *1733*, 020035.
35. Kudelski, A.; Grochala, W.; Janik-Czachor, M.; Bukowska, J.; Szummer, A.; Dolata, M. Surface-enhanced Raman scattering (SERS) at Copper(I) oxide. *J. Raman Spectrosc.* **1998**, *29*, 431–435. [[CrossRef](#)]
36. Amendola, V.; Rizzi, G.A.; Polizzi, S.; Meneghetti, M. Synthesis of Gold Nanoparticles by Laser Ablation in Toluene: Quenching and Recovery of the Surface Plasmon Absorption. *J. Phys. Chem. B* **2005**, *109*, 23125–23128. [[CrossRef](#)] [[PubMed](#)]

37. Nikov, R.G.; Nedyalkov, N.N.; Atanasov, P.A.; Karashanova, D.B. Laser-assisted fabrication and size distribution modification of colloidal gold nanostructures by nanosecond laser ablation in different liquids. *Appl. Phys. A* **2017**, *123*, 490. [[CrossRef](#)]
38. Cho, H.-G. Matrix Infrared Spectra and DFT Computations of CH₂CNH and CH₂NCH Produced from CH₃CN by Laser-Ablation Plume Radiation. *Bull. Korean Chem. Soc.* **2013**, *34*, 1361–1365. [[CrossRef](#)]
39. Andrews, L.; Citra, A. Infrared Spectra and Density Functional Theory Calculations on Transition Metal Nitrosyls. Vibrational Frequencies of Unsaturated Transition Metal Nitrosyls. *Chem. Rev.* **2002**, *102*, 885–912. [[CrossRef](#)]
40. Cho, H.-G.; Andrews, L. Matrix Infrared Spectra and Density Functional Calculations of the H₂CCN and H₂CNC Radicals Produced from CH₃CN. *J. Phys. Chem. A* **2011**, *115*, 8638–8642. [[CrossRef](#)]
41. Amendola, V.; Meneghetti, M. What controls the composition and the structure of nanomaterials generated by laser ablation in liquid solution? *Phys. Chem. Chem. Phys.* **2013**, *15*, 3027–3046. [[CrossRef](#)] [[PubMed](#)]
42. Hamad, S.; Podagatlapalli, G.K.; Rao, S.V.; Syed, H.; Soma, V.R. Explosives Detection with Copper Nanostructures Fabricated using Ultrafast Laser Ablation in Acetonitrile. *Light Energy Environ.* **2014**. [[CrossRef](#)]
43. Kessler, F.K.; Zheng, Y.; Schwarz, D.; Merschjann, C.; Schnick, W.; Wang, X.; Bojdys, M.J. Functional carbon nitride materials—Design strategies for electrochemical devices. *Nat. Rev. Mater.* **2017**, *2*, 17030. [[CrossRef](#)]
44. Miller, T.; Jorge, A.B.; Suter, T.M.; Sella, A.; Corà, F.; McMillan, P.F. Carbon nitrides: Synthesis and characterization of a new class of functional materials. *Phys. Chem. Chem. Phys.* **2017**, *19*, 15613–15638. [[CrossRef](#)] [[PubMed](#)]
45. Wen, J.; Xie, J.; Chen, X.; Li, X. A review on g-C₃N₄-based photocatalysts. *Appl. Surf. Sci.* **2017**, *391*, 72–123. [[CrossRef](#)]
46. Mansor, N.; Miller, T.S.; Dedigama, I.; Jorge, A.B.; Jia, J.; Brázdová, V.; Mattevi, C.; Gibbs, C.; Hodgson, D.; Shearing, P.R.; et al. Graphitic Carbon Nitride as a Catalyst Support in Fuel Cells and Electrolyzers. *Electrochim. Acta* **2016**, *222*, 44–57. [[CrossRef](#)]
47. Algara-Siller, G.; Severin, N.; Chong, S.Y.; Björkman, T.; Palgrave, R.G.; Laybourn, A.; Antonietti, M.; Khimiyak, Y.Z.; Krashennnikov, A.V.; Rabe, J.P.; et al. Triazine-Based Graphitic Carbon Nitride: A Two-Dimensional Semiconductor. *Angew. Chem.* **2014**, *126*, 7580–7585. [[CrossRef](#)]
48. Wirnhier, E.; Doblinger, M.; Gunzelmann, D.; Senker, J.; Lotsch, B.V.; Schnick, W. Poly(triazine imide) with intercalation of lithium and chloride ions [(C₃N₃)₂(NHxLi_{1-x})₃•LiCl]: A crystalline 2D carbon nitride network. *Chem. Eur. J.* **2011**, *17*, 3213–3221. [[CrossRef](#)]
49. Ladva, S.A.; Travis, W.; Quesada-Cabrera, R.; Rosillo-Lopez, M.; Afandi, A.; Li, Y.; Jackman, R.B.; Bear, J.C.; Parkin, I.P.; Blackman, C.; et al. Nanoscale, conformal films of graphitic carbon nitride deposited at room temperature: A method for construction of heterojunction devices. *Nanoscale* **2017**, *9*, 16586–16590. [[CrossRef](#)]
50. Suter, T.M.; Brazdova, V.; McColl, K.; Miller, T.S.; Nagashima, H.; Salvadori, E.; Sella, A.; Howard, C.A.; Kay, C.W.M.; Cora, F.; et al. Synthesis, Structure and Electronic Properties of Graphitic Carbon Nitride Films. *J. Phys. Chem. C* **2018**, *122*, 25183–25194. [[CrossRef](#)]
51. Zhang, Z.J.; Fan, S.; Lieber, C.M. Growth and composition of covalent carbon nitride solids. *Appl. Phys. Lett.* **1995**, *66*, 3582–3584. [[CrossRef](#)]
52. Rodil, S.E.; Muhl, S.; Maca, S.; Ferrari, A. Optical gap in carbon nitride films. *Thin Solid Films* **2003**, *433*, 119–125. [[CrossRef](#)]
53. Inagaki, M.; Toyoda, M.; Soneda, Y.; Morishita, T. Nitrogen-doped carbon materials. *Carbon* **2018**, *132*, 104–140. [[CrossRef](#)]
54. González, P.; Soto, R.; Parada, E.; Redondas, X.; Chiussi, S.; Serra, J.; Pou, J.; Leon, B.; Pérez-Amor, M. Carbon nitride films prepared by excimer laser ablation. *Appl. Surf. Sci.* **1997**, *109*, 380–383. [[CrossRef](#)]
55. Bulíř, J.; Jelínek, M.; Vorlíček, V.; Zemek, J.; Perina, V. Study of nitrogen pressure effect on the laser-deposited amorphous carbon films. *Thin Solid Films* **1997**, *292*, 318–323. [[CrossRef](#)]
56. Zhao, X.; Ong, C.W.; Tsang, Y.C.; Wong, Y.W.; Chan, P.W.; Choy, C.L. Reactive pulsed laser deposition of CN_x films. *Appl. Phys. Lett.* **1995**, *66*, 2652–2654. [[CrossRef](#)]
57. Ong, C.W.; Zhao, X.-A.; Tsang, Y.; Choy, C.; Chan, P. Effects of substrate temperature on the structure and properties of reactive pulsed laser deposited CN_x films. *Thin Solid Films* **1996**, *280*, 1–4. [[CrossRef](#)]
58. Alexandrescu, R.; Huisken, F.; Pugna, G.; Crunteanu, A.; Petcu, S.; Cojocaru, S.; Cireasa, R.; Morjan, I.; Cojocaru, C.S. Preparation of carbon nitride fine powder by laser induced gas-phase reactions. *Appl. Phys. A* **1997**, *65*, 207–213. [[CrossRef](#)]

59. Sharma, A.K.; Ayyub, P.; Multani, M.S.; Adhi, K.P.; Ogale, S.B.; Sunderaraman, M.; Upadhyay, D.D.; Banerjee, S. Synthesis of crystalline carbon nitride thin films by laser processing at a liquid–solid interface. *Appl. Phys. Lett.* **1996**, *69*, 3489–3491. [[CrossRef](#)]
60. Yang, L.; May, P.W.; Yin, L.; Brown, R.; Scott, T.B. Direct Growth of Highly Organized Crystalline Carbon Nitride from Liquid-Phase Pulsed Laser Ablation. *Chem. Mater.* **2006**, *18*, 5058–5064. [[CrossRef](#)]
61. Li, H.; Xu, Y.; Sitinamaluwa, H.; Wasalathilake, K.; Galpaya, D.; Yan, C. Cu nanoparticles supported on graphitic carbon nitride as an efficient electrocatalyst for oxygen reduction reaction. *Chin. J. Catal.* **2017**, *38*, 1006–1010. [[CrossRef](#)]
62. Le, S.; Fang, B.; Jiang, T.; Zhao, Q.; Liu, X.; Li, Y.; Gong, M. Cu-doped mesoporous graphitic carbon nitride for enhanced visible-light driven photocatalysis. *RSC Adv.* **2016**, *6*, 38811–38819. [[CrossRef](#)]
63. Muniandy, L.; Adam, F.; Mohamed, A.R.; Iqbal, A.; Rahman, N.R.A. Cu²⁺ coordinated graphitic carbon nitride (Cu-g-C₃N₄) nanosheets from melamine for the liquid phase hydroxylation of benzene and VOCs. *Appl. Surf. Sci.* **2017**, *398*, 43–55. [[CrossRef](#)]
64. Gao, J.; Wang, J.; Qian, X.; Dong, Y.; Xu, H.; Song, R.; Yan, C.; Zhu, H.; Zhong, Q.; Qian, G.; et al. One-pot synthesis of copper-doped graphitic carbon nitride nanosheet by heating Cu–melamine supramolecular network and its enhanced visible-light-driven photocatalysis. *J. Solid State Chem.* **2015**, *228*, 60–64. [[CrossRef](#)]
65. Tahir, B.; Tahir, M.; Amin, N.A.S. Photo-induced CO₂ reduction by CH₄/H₂O to fuels over Cu-modified g-C₃N₄ nanorods under simulated solar energy. *Appl. Surf. Sci.* **2017**, *419*, 875–885. [[CrossRef](#)]
66. Shi, G.; Yang, L.; Liu, Z.; Chen, X.; Zhou, J.; Yu, Y. Photocatalytic reduction of CO₂ to CO over copper decorated g-C₃N₄ nanosheets with enhanced yield and selectivity. *Appl. Surf. Sci.* **2018**, *427*, 1165–1173. [[CrossRef](#)]
67. Wolosiuk, A.; Tognalli, N.G.; Martínez, E.D.; Granada, M.; Fuertes, M.C.; Troiani, H.; Bilmes, S.A.; Fainstein, A.; Soler-Illia, G.J.A.A. Silver Nanoparticle-Mesoporous Oxide Nanocomposite Thin Films: A Platform for Spatially Homogeneous SERS-Active Substrates with Enhanced Stability. *ACS Appl. Mater. Interfaces* **2014**, *6*, 5263–5272. [[CrossRef](#)] [[PubMed](#)]
68. Yang, K.-H.; Liu, Y.-C.; Hsu, T.-C.; Juang, M.-Y. Strategy to improve stability of surface-enhanced raman scattering-active Ag substrates. *J. Mater. Chem.* **2010**, *20*, 7530–7535. [[CrossRef](#)]
69. Mai, F.-D.; Yang, K.-H.; Liu, Y.-C.; Hsu, T.-C. Improved stabilities on surface-enhanced Raman scattering-active Ag/Al₂O₃ films on substrates. *Analyst* **2012**, *137*, 5906–5912. [[CrossRef](#)] [[PubMed](#)]
70. Jiang, J.; Zhu, L.; Zou, J.; Ou-Yang, L.; Zheng, A.; Tang, H. Micro/nano-structured graphitic carbon nitride—Ag nanoparticle hybrids as surface-enhanced Raman scattering substrates with much improved long-term stability. *Carbon* **2015**, *87*, 193–205. [[CrossRef](#)]
71. Jiang, J.; Zou, J.; Wee, A.T.S.; Zhang, W. Use of Single-Layer g-C₃N₄/Ag Hybrids for Surface-Enhanced Raman Scattering (SERS). *Sci. Rep.* **2016**, *6*, 34599. [[CrossRef](#)] [[PubMed](#)]
72. Schneider, C.A.; Rasband, W.S.; Eliceiri, K.W. NIH Image to ImageJ: 25 years of Image Analysis. *Nat. Methods* **2012**, *9*, 671–675. [[CrossRef](#)] [[PubMed](#)]
73. Biesinger, M.C.; Payne, B.P.; Grosvenor, A.P.; Lau, L.W.; Gerson, A.R.; Smart, R.S. Resolving surface chemical states in XPS analysis of first row transition metals, oxides and hydroxides: Cr, Mn, Fe, Co and Ni. *Appl. Surf. Sci.* **2011**, *257*, 2717–2730. [[CrossRef](#)]
74. Liu, P.; Wang, H.; Li, X.; Rui, M.; Zeng, H. Localized surface plasmon resonance of Cu nanoparticles by laser ablation in liquid media. *RSC Adv.* **2015**, *5*, 79738–79745. [[CrossRef](#)]
75. Zambon, A.; Mouesca, J.M.; Gheorghiu, C.; Bayle, P.A.; Pécaut, J.; Claeys-Bruno, M.; Gambarelli, S.; Dubois, L. s-Heptazine oligomers: Promising structural models for graphitic carbon nitride. *Chem. Sci.* **2016**, *7*, 945–950. [[CrossRef](#)] [[PubMed](#)]
76. Fina, F.; Callear, S.K.; Carins, G.M.; Irvine, J.T.S. Structural Investigation of Graphitic Carbon Nitride via XRD and Neutron Diffraction. *Chem. Mater.* **2015**, *27*, 2612–2618. [[CrossRef](#)]
77. Tyborski, T.; Merschjann, C.; Orthmann, S.; Yang, F.; Lux-Steiner, M.-C.; Schedel-Niedrig, T. Crystal structure of polymeric carbon nitride and the determination of its process-temperature-induced modifications. *J. Phys. Condens. Matter* **2013**, *25*, 395402. [[CrossRef](#)]
78. Bonner, O.; Curry, J.D. Infrared spectra of liquid H₂O and D₂O. *Infrared Phys.* **1970**, *10*, 91–94. [[CrossRef](#)]
79. Rodil, S.E.; Ferrari, A.; Robertson, J.; Muhl, S. Infrared spectra of carbon nitride films. *Thin Solid Films* **2002**, *420*, 122–131. [[CrossRef](#)]

80. Ferrari, A.C.; Rodil, S.E.; Robertson, J. Interpretation of infrared and Raman spectra of amorphous carbon nitrides. *Phys. Rev. B* **2003**, *67*, 155306. [[CrossRef](#)]
81. Angeloni, L.; Smulevich, G.; Marzocchi, M.P. Resonance Raman spectrum of crystal violet. *J. Raman Spectrosc.* **1979**, *8*, 305–310. [[CrossRef](#)]
82. Anastasopoulos, J.; Beobide, A.S.; Manikas, A.; Voyiatzis, G. Quantitative surface-enhanced resonance Raman scattering analysis of methylene blue using silver colloid. *J. Raman Spectrosc.* **2017**, *48*, 1762–1770. [[CrossRef](#)]
83. Mo, Y.; Lei, J.; Li, X.; Wächter, P. Surface enhanced Raman scattering of rhodamine 6G and dye 1555 adsorbed on roughened copper surfaces. *Solid State Commun.* **1988**, *66*, 127–131. [[CrossRef](#)]
84. Ujihara, M.; Dang, N.M.; Imae, T. Surface-Enhanced Resonance Raman Scattering of Rhodamine 6G in Dispersions and on Films of Confeito-Like Au Nanoparticles. *Sensors* **2017**, *17*, 2563. [[CrossRef](#)] [[PubMed](#)]
85. Le Ru, E.C.; Blackie, E.; Meyer, M.; Etchegoin, P.G. Surface Enhanced Raman Scattering Enhancement Factors: A Comprehensive Study. *J. Phys. Chem. C* **2007**, *111*, 13794–13803. [[CrossRef](#)]
86. Jiang, L.; You, T.; Yin, P.; Shang, Y.; Zhang, D.; Guo, L.; Yang, S. Surface-enhanced Raman scattering spectra of adsorbates on Cu₂O nanospheres: Charge-transfer and electromagnetic enhancement. *Nanoscale* **2013**, *5*, 2784–2789. [[CrossRef](#)] [[PubMed](#)]
87. He, S.; Chua, J.; Tan, E.K.M.; Kah, J.C.Y. Optimizing the SERS enhancement of a facile gold nanostar immobilized paper-based SERS substrate. *RSC Adv.* **2017**, *7*, 16264–16272. [[CrossRef](#)]
88. Xu, Y.; Konrad, M.P.; Trotter, J.L.; McCoy, C.P.; Bell, S.E.J. Rapid One-Pot Preparation of Large Freestanding Nanoparticle-Polymer Films. *Small* **2016**, *13*, 1602163. [[CrossRef](#)] [[PubMed](#)]
89. Su, S.; Zhang, C.; Yuwen, L.; Chao, J.; Zuo, X.; Liu, X.; Song, C.; Fan, C.; Wang, L. Creating SERS Hot Spots on MoS₂ Nanosheets with in Situ Grown Gold Nanoparticles. *ACS Appl. Mater. Interfaces* **2014**, *6*, 18735–18741. [[CrossRef](#)]



© 2019 by the authors. Licensee MDPI, Basel, Switzerland. This article is an open access article distributed under the terms and conditions of the Creative Commons Attribution (CC BY) license (<http://creativecommons.org/licenses/by/4.0/>).